Science
AAAS

Supplementary Materials for

High-resolution mapping of losses and gains of Earth's tidal wetlands

Nicholas J. Murray *et al*.

Corresponding author: Nicholas J. Murray, nicholas.murray@jcu.edu.au

Science **376**, 744 (2022)
DOI: 10.1126/science.abm9583

The PDF file includes:

Materials and Methods
Figs. S1 to S9
Tables S1 to S10
References

Other Supplementary Material for this manuscript includes the following:

MDAR Reproducibility Checklist

Materials and Methods

1. Overview

This study establishes a framework for mapping the distribution and change of the world's tidal wetlands with satellite image archives and biophysical data. Tidal wetlands in our study collectively refer to three of the world's most extensive intertidal ecosystem types: tidal flats, tidal marshes and mangroves (*8*, *12*, *31*). These three intertidal ecosystem types are regularly inundated throughout the tidal cycle correspond to the IUCN Global Ecosystem Typology (*32*) descriptions for muddy shorelines (typology code MT1.2; hereafter 'tidal flats'*)*, coastal tidal marshes and reedbeds (MFT1.3; hereafter 'tidal marshes') and intertidal forests and shrublands (MFT1.2; hereafter 'mangroves'). In this study tidal flats are represented as fine to coarse particle-sized sediment and sand dominated ecosystems that are regularly inundated throughout the tidal cycle and occur primarily on low-sloping, low energy coastlines (*9*, *33*), tidal marshes as salt-tolerant forbs, grasses and shrubs that occur in intertidal environments (*34*), and mangroves as structurally complex intertidal forests that occur mainly in warm regions (Figure S1) (*35*).

Vague distribution boundaries between intertidal ecosystems present a considerable challenge for remote sensing analyses of coastal ecosystems. Remote sensing studies can over- or under-estimate the extent of single ecosystems due to continuous ecotones among each ecosystem type, the occurrence of complex ecosystem mosaics at a range of spatial scales within the intertidal zone, variable vegetation height within vegetated coastal ecosystems, limited height development of tree species on some substrates, sparse vegetation cover, the dynamic movement of ecotones over time, and varying tidal inundation at the time of remote observation. These issues tend to result in gaps or overlaps in independently developed maps of coastal ecosystems, limiting their ability to be used for integrated analyses of global tidal wetland dynamics. To address this, we developed a three-stage classification workflow for earth observation data that sought to (i) estimate the occurrence of the three intertidal ecosystems in a single map class ('tidal wetlands') for seven time-steps between 1999 and 2019 (Stage 1), (ii) detect and classify their change over the full 20-year study period (Stage 2), and (iii) classify tidal wetland changes into their component intertidal ecosystem type (tidal flats, tidal marsh or mangroves) and identify when the change occurred (Stage 3).

Machine learning classifiers have been transformative for global-scale models of the distribution of land cover, largely because of their effectiveness at handling large and complex feature sets, ability to be deployed in parallel, and demonstrated high predictive performance across a wide range of applied remote sensing analyses (*36*). They have therefore been used to map the extent of several intertidal ecosystems, including tidal flats (*9*) and mangroves (*13*). For this reason, random forest classifiers were applied at in the three stages of our analysis, using training datasets developed for each and a set of multitemporal data layers as covariates. The models were applied to coastal areas between 60°N and 60°S. To reduce unnecessary analyses within these latitudinal bounds, the analysis was limited to the maximum area represented by the following criteria: less than 40-m water depth (*37*), less than 40-m elevation (*37*), within 5-km of any intertidal ecosystems mapped in existing global-scale maps of single ecosystems (*9*, *13*, *15*, *38*, *39*), or less than 5-km to the coastline (*40*). We ran our remote sensing analysis end-to-end in Google Earth Engine (*41*) and used *R* (*42*) to conduct model tuning and develop data summaries. Model code is available as Supplementary Data S1 and the training data and map data products as Supplementary Data S2 and S3.

2. Covariate data

The Landsat Thematic Mapper (TM), Enhanced Thematic Mapper + (ETM+) and Operational Land Imager (OLI) instruments on Landsat 5–8 satellites are amongst the most important data sources for investigating broad-scale dynamics of the Earth's ecosystems (*43-45*). Landsat Collection-1 At-Surface Reflectance data (*46*) were used to produce a set of time-series covariate layers that formed the basis of the three stages of our modelling approach. We collected every Landsat archive image acquired over the study area between 1999 and 2019 (1,166,385 images), masked cloud and cloud shadow pixels (*46*), and summarized them into cloud-free temporal composite metric layers over seven 3-yearly periods (1999–2001, 2002–2004, 2005–2007, 2008–2010, 2011–2013, 2014–2016, 2017–2019). Composite metrics are useful for minimizing contamination by cloud, cloud shadow and snow, characterizing the extent of tidal influence detectable by satellite sensors, and representing diverse aspects of coastal and vegetation dynamics in an efficient manner suitable for use in regional to global-scale classification models (*9*, *26*, *47*, *48*). Analysis time-steps were timed with the launch of the Landsat 7 ETM + instrument and were fixed to three-year periods (*49, 50*). This balanced the requirement for data products of sufficient temporal resolution to investigate intertidal ecosystem dynamics against the need to use a sufficient number of satellite images to generate cloud-free composite metrics across the global intertidal area (*49*, *50*). For each three-year time-period, 88 composite metric layers were generated from the Landsat Archive data to serve as spectral covariates in the three classification models. Pixels where a lack of cloud-free observations precluded change classification accounted for only 1.7% of the total mapped area. To promote accurate predictions of the occurrence of tidal wetlands (Stage 1) and their component ecosystem types (Stage 3), we also developed additional covariate layers of biophysical variables known to influence local and global distributions of tidal wetlands (*9*, *28, 51*, *52*), including air temperature and elevation. The complete list of covariate layers is presented in Supplementary Table S1.

<u>3. Intertidal ecosystem training data</u>

We developed a globally distributed training dataset for modelling the extent of tidal wetlands and their component intertidal ecosystems. This was achieved through visual interpretation of high-resolution satellite images available from Google Earth, Bing Maps and other mapping platforms (such as Planet Basemaps) in combination with the full set of cloud-free Landsat composite metrics (Table S1). Typically, pixels included in the training set met the following conditions: (i) a clear presence of distinguishing features of each ecosystem type, such as mangrove trees, tidally inundated sediments, or marsh vegetation, (ii) located along the visible natural coastline where intertidal ecosystems are clearly observable, and (iii) the ecosystem was confirmed as present in the reference period (2014–2016). Where possible, other sources of information, including from published studies, coastal atlases and publicly available datasets, were used to aid image interpretation. Image analysts also used their experience and knowledge of the visual characteristics of each ecosystem type to inform their collection of training data and did not include records where there was any uncertainty about the ecosystem type or its presence during the reference period. This resulted in a tidal wetland training dataset of 23,138 occurrence records annotated with ecosystem type (tidal flat, tidal marsh or mangrove). Furthermore, 17,747 occurrence records of non-tidal wetland land cover types were collected to enable separation from other land cover types that occur in the coastal zone (‘permanent water’ and ‘terrestrial other’; Figure S2). The permanent water class included records from deep water and shallow marine ecosystems, including kelp forests, seagrass meadows and photic coral reefs. The terrestrial other class included a variety of land cover types ranging from agriculture and settlements to sandy shorelines and supra-littoral coastal ecosystems. Our ground-up compilation of training data, as opposed to the sampling of existing publicly available map products, reduces error propagation among global map products and enables the inclusion of training data from areas that are unmapped in existing global map datasets

3. Distribution of tidal wetlands

The Stage 1 random-forest classification model aimed to estimate the global distribution of tidal wetlands, formulated as the combined distribution of the three intertidal ecosystem types represented in our training set. The 'tidal wetland' category comprised the training data of the three intertidal ecosystems, with the 'permanent water' and 'terrestrial other' records combined and used as absence data. The covariate layers (Table S1) were sampled for the reference time period (2014–2016) at the location of each record in the training set. We sought to reduce model complexity by removing highly correlated covariates, however, model testing with the training set indicated that lowest out-of-bag error rates were achieved with the full covariate set. Prior to deploying the classification model in Google Earth Engine, model hyper-parameters were optimized by exploring a hypergrid search space with the training set in *R* using the package 'ranger' (*53*). The hypergrid search consisted of 240 simulations with varying parameter values of the number of trees grown, the number of covariates sampled at each split, the fraction of observations sampled at each split, and the minimum node size. Parameter values deployed in Earth Engine across the full global study area were the mean of the top ten models identified by lowest out-of-bag error rate in the hypergrid simulation. We predicted the global distribution of tidal wetlands for each of the seven time-periods by running random forests in probability mode, which represents the agreement of random forest decision trees, and yields per-pixel tidal wetland probability layers for each time period (*41*).

Owing to similar inundation dynamics, distinguishing low-elevation coastal aquaculture from coastal ecosystems remains a key challenge of coastal remote sensing. Initial model runs indicated commission error with coastal aquaculture, particularly in Java and Vietnam. For this reason, we developed a mask of South-east Asian aquaculture using maps developed of this land cover type for the start year of our analysis in 1999 (*54*). Commission error was also reduced by using the global training set to estimate the ecosystem type of each tidal wetland pixel above 10-m elevation (*52*), corresponding to the maximum elevation of these ecosystems in our training set, masking those estimated as tidal marsh or tidal flat, as well as pixels identified as mangroves that occurred outside of the mangrove habitat layer developed by Global Mangrove Watch program (*13*). After applying these masks, tidal wetland extent maps were obtained by applying a threshold of 0.5 to the tidal wetland probability layers and then post-processed to a minimum mapping unit of 10 eight-way connected 30×30-m pixels.

5. Tidal wetland change product

The overarching aim of our study was to investigate global tidal wetland change over a 20-year period. Although the Stage 1 tidal wetland extent model was designed to deliver extent maps that met stringent quality aspirations, variation in the number of images available per region and known limitations of change maps developed from optical remote sensing can lead to year-on-year variation in mapped extent related to model error and noise, rather than observed changes (*55*-*58*). We therefore developed a second classification model to classify pixels where image differencing the tidal wetland extent products suggested disturbance events may have occurred during the study period (Stage 2).

We developed an additional global training set for this purpose with a stratified random sample of 950 points in disturbance patches identified by differencing the first (1999–2001) and last (2017–2019) year of the tidal wetland extent products. We used high-resolution historical imagery from the Google Earth Pro time-slider and the Landsat composite metrics from 1999–2001 and 2017–2019 to annotate each training point according to whether loss, gain or no change was evident over the 20-year study period. Tidal wetland loss was defined as the replacement, at the 30-m pixel scale, of any of the three focal intertidal ecosystems with non-intertidal ecosystems. Tidal wetland gain was defined as the establishment of any of the three intertidal ecosystems in pixels where they did not occur in 1999. According to these definitions, tidal wetland loss and gain training points were included without explicit knowledge of specific change drivers, and therefore included records resulting from diverse change drivers ranging from direct losses due to reclamation, seawalls, dikes, vegetation cutting, mowing, and agricultural development, to die back caused by drivers such as pollution, permanent inundation or altered inundation dynamics. In all cases, pixels labelled as loss indicated a clear loss of defining features of each ecosystem in imagery between the start to the end of the study period while pixels labelled as gain indicated the presence of new intertidal ecosystems that were initially mapped as terrestrial (non-tidal) or permanent open water. Sample pixels where no change was observed were labeled as no change, and any pixels that could not be allocated to a change class due to insufficient historical imagery were excluded from the sample set. Stratified random samples were drawn and assessed in blocks (~500 points), with a sensitivity analysis performed after each block to determine whether the sample size was sufficient to stabilize the overall accuracy estimate. The sensitivity analysis involved a bootstrap resampling approach that simulated an increasing number of validation samples, recording the variance of the accuracy estimate. Similarly to a previous study (*9*), we determined that there were enough validation samples once the variance stabilized such that adding more samples did not significantly change estimates or uncertainty levels. The training set was supplemented over model iterations with manually acquired samples in areas that represented the most challenging situations of confirmed change. The final training set for the change classifier comprised 1,787 points that represented losses (638 points), gains (457 points) and no change (692 points) of tidal wetlands over the 20 year study period (Figure S3).

For covariates, we computed the difference in pixel values from our Landsat covariate set between the start (1999–2001) and end of the time series (2017–2019; 88 covariates; Table S2). A covariate layer representing the tidal wetland trend was also included by developing a per-pixel linear model fit to the seven per-pixel probability layers of global tidal wetland extent (one covariate; Table S2). We applied the change classification model to all disturbance patches, yielding a global map of pixels depicting losses and gains of tidal wetlands between 1999 and 2019.

To annotate the type of loss or gain, we applied a third random forest classifier to each gain or loss pixel (Stage 3). The intertidal ecosystem type lost or gained was estimated using the covariates for the initial (1999–2001; intertidal ecosystem type in loss patches) and final model time steps (2017–2019; intertidal ecosystem type in gain patches), and the intertidal ecosystem training set (n = 17,772 records). The year of loss or gain ('lossyear' and 'gainyear') was computed as the last or first time-step that a pixel classified as tidal wetland was present in the time series. The change map was post-processed to a minimum mapping unit of 10 eight-way connected 30×30-m pixels and removed obvious classification errors. The final outputs from the analysis were a set of global maps, at 30-m resolution, depicting the estimated global extent of tidal wetlands since 1999, the distribution of tidal wetland losses and gains by intertidal ecosystem type, and the time-step that the loss or gain event was estimated to have occurred (Figure S4).

6. Validation and uncertainty estimates

As noted in many global-scale studies, validation of any land cover maps and their change is extremely challenging (*26*, *48*). Errors of omission and commission can arise from model misclassification of dynamic features (e.g., turbid water), insufficient representation of target features in training data, inappropriate formulation of map classification schemes, coarse resolution covariate data that can cause unreliable classifications of features at subpixel scales, and the presence of unmapped features that occur at spatial scales smaller than the minimum mapping unit (*58-60*). We followed convention and employed independent, high spatial resolution satellite data that matched the temporal span of our products to validate the model outputs. Here, we leveraged the growing archive of historical high-resolution imagery available in Google Earth Pro and visualizations of Landsat Archive data to evaluate the accuracy of the tidal wetland extent map (2017–2019) and of the change product (1999–2019). For each validation exercise, we used established practices for assessments of land cover and land cover change to generate validation sets and used these to independently quantify map error and bias of our map products (*57, 59, 61, 62*). We ensured sufficient sample size of the two validation sets with sensitivity analyses to identify the point at which further samples in the validation set would not alter accuracy results outside of a 95% confidence interval (*9, 63*). This process yielded two validation sets developed from stratified random sampling, (i) the extent validation set, consisting of map classes 'tidal wetland' and 'other' (n =1,359 validation points; Figure S5) and (ii) the change validation set of map classes 'stable', 'gain' and 'loss'(n = 3,060 validation points; Figure S6).

To independently annotate validation points in the two validation sets, we developed an online accuracy assessment application in Google Earth Engine (*41*) that enabled an experienced analyst to concurrently view a relevant set of up to four images for each validation sample. Images available to the analyst included a subset of the time-series Landsat covariates visualized as the Near-Infrared Band, a true color composite, a false color composite, and the standard deviation of the Normalized Difference Water Index (NDWI; *64*), the Modified Normalized Difference Water Index (MNDWI; *65*) and the Automated Water Extraction Index (AWEI; *66*) over the 2017–2019 -year period. The analyst also used Google Earth Pro (including the time-slider function), Bing Maps, and any other information source, including map figures in published papers that enabled an independent assessment of each validation sample.

We used the validation datasets to calculate standard map accuracy metrics, and used newly developed resampling protocols that been shown to be effective for classification analyses of vegetation distributions (*67*) and coastal ecosystem extents (*9*) to estimate map accuracies and confidence intervals. Bootstrapping was performed by resampling the validation samples using 1000 iterations, taking the mean of the sampling distribution as the reported accuracy value and the 0.025 and 0.975 percentiles of the sampling distribution as the 95% confidence interval. Bootstrapping routines yielded accuracy estimates (mean and 95% confidence interval) for the tidal wetland extent and change products (Tables S5-S8).

Traditionally, uncertainty estimates are generated via parametric methods that yield symmetrical confidence intervals around accuracy and area estimates. However, maps derived from remote sensing classifications tend to have uneven omission and commission error due to factors including covariate data quality (such as arising from cloud or smoke haze), sensitivity to tidal dynamics, different spectral similarities among classes, spatiotemporal variation in land cover change, and other uncertainties related to model performance (*57, 58, 61, 62, 67, 68*). Our validation results indicated asymmetry between omission and commission error (Tables S5-S8). To allow propagation of this asymmetry into our estimates of global extent, we used the 95% interval on the resampled distribution of omission and commission errors to estimate the upper and lower bounds for the area estimates of the tidal wetland class, such that:

$$area_i \ \mathbf{95\%}\boldsymbol{CI}_{lower} = area_i - (area_i * \ commission \ \boldsymbol{P}_{95})$$

$$area_i \ \mathbf{95\%}\boldsymbol{CI}_{upper} = area_i + (area_i * omission \ \boldsymbol{P}_{95})$$

where $area_i$ is the mapped area value for the tidal wetland class i, and $\boldsymbol{P}_{95}$ is the 95% percentile of the commission/omission error corresponding to tidal wetland class i. Calculating confidence intervals in this manner can result in uneven intervals, but this is a more objective representation of uncertainty for end-users given known asymmetry in commission and omission errors in the map products.

We calculated confidence intervals for the loss and gain estimates for each intertidal ecosystem class using a similar approach, except that the error was multiplicative between the ecosystem class and the change class. For loss estimates,

$$loss_i\ \mathbf{95\%}\boldsymbol{CI}_{lower} = loss_i - \left(loss_i * \ lower_{i,loss}\right)$$

$$loss_i\ \mathbf{95\%}\boldsymbol{CI}_{upper} = loss_i + \left(loss_i * \ upper_{i,loss}\right)$$

where $loss_i$ is the mapped area estimate of class *i* (one of mangrove, tidal marsh or tidal flat) intersected with the loss class in the change product, and

$$lower_{i,loss} = \left(1 - \left((1 - \ commission\ \boldsymbol{P}_{95,i}) * (1 - commission\ \boldsymbol{P}_{95,loss})\right)\right)$$

$$upper_{i,loss} = \left(1 - \left((1 - \ omission\ \boldsymbol{P}_{95,i}) * (1 - commission\ \boldsymbol{P}_{95,loss})\right)\right)$$

where $\boldsymbol{P}_{95,i}$ is the 95th percentile of the commission/omission error for the intertidal ecosystem class *i*, and $\boldsymbol{P}_{95,loss}$ is the 95th percentile of the commission error for the loss class in the change product. The same process was applied for the gain estimates (i.e., replacing loss with gain above). Although this approach considerably widens confidence intervals in derived area estimates, particularly for change estimates of individual ecosystem types, it reflects the dynamic nature of tidal wetlands and the complexities of detecting their change.

<u>7. Tidal wetland analysis.</u>

We estimated the area of the tidal wetland extent and change products and summarized the results at several spatial scales, including global, continental, by country (*69*) (Table S3), and for particular regions of interest, such as the world's 100 largest deltas (*19*) and marine ecoregions (*70*). To investigate the extent of transitions among ecosystems, we also estimated the area of tidal wetlands that changed from one ecosystem type to another (e.g., from tidal flat to mangrove) over the study period (1999–2019). For example, a pixel within the tidal wetland extent map estimated as tidal flat in 1999 but mapped as mangrove in 2019 was flagged as a tidal flat to mangrove transition (Table S4). Only pixels that were mapped as tidal wetlands at the start and end of the study periods (i.e., not lost or gained over the 20 year period) were considered to be transition pixels.

8. Direct and indirect driver analysis

The causes of tidal wetland change are complex and are often the result of synergistic, interacting and/or multiplicative processes that operate at a range of spatial scales. Several studies have attempted to attribute the conversion of mangroves to other land cover types to anthropogenic (human-driven) and natural drivers (*14, 71*). Anthropogenic drivers are typically related to direct human activities (including conversion to aquaculture and other commodities, urban land uses and infrastructure development). Natural drivers typically include erosion, sediment deposition, sea level rise, and other natural coastal processes, which may be influenced by climate change and remote human-induced land-use changes whose origin may be tens or hundreds of kilometers from the observed change event. These drivers of coastal change operate at local to global scales and complex interactions and synergies are evident worldwide. Disentangling 'natural' and 'anthropogenic' drivers of change is therefore extremely challenging (*72*).

Here we develop a sample-based estimate (*26*) of the relative contribution of direct human activities (such as conversion to aquaculture, agriculture, urban development) and indirect drivers (representing the combined effect of climate change, natural coastal processes, and other remote drivers of change) to the losses and gains of tidal wetlands that were detected by our remote sensing analysis. For this, a global weighted probability sample over the tidal wetland change data was developed to estimate the proportion of direct and indirect drivers on the following tidal wetland change dynamics:

(i) Tidal flat gain;
(ii) Tidal flat loss;
(iii) Tidal marsh gain;
(iv) Tidal marsh loss;
(v) Mangrove gain; and
(vi) Mangrove loss.

For each change dynamic, we sampled 250 3 × 3 kilometer grid cells with a weighted probability proportional to the area of tidal wetland change for the corresponding change dynamic detected within each grid cell. Within each sampled grid cell, we randomly sampled a loss or gain pixel (30-m) that matched the sampled change dynamic of the grid cell (e.g., tidal marsh gain). For each sampled pixel, we created polygon features representing the boundary of the pixel (30-m) for high-resolution image interpretation and an image chip boundary an order of magnitude larger (300-m) for scale reference (Figure S8).

We imported the pixel boundaries into Google Earth Pro and used high-resolution images and the time-slider tool to inspect available high-resolution imagery before, during and after the 1999–2019 study period to assess the drivers of tidal wetland change at the 30-m pixel scale. Changes attributed to direct drivers were associated with visible land changes such as aquaculture, agriculture, plantations, urban and industrial development, and other artificial objects such as coastal infrastructure (bridges and dikes). The impact of indirect drivers was assumed where samples could not be attributed to a direct driver of change (Figure S8). Samples where clear attribution to the two driver classes was not possible due to lack of imagery or uncertainty about tidal wetland change were removed from the sample set. The relative contribution of direct and indirect drivers of tidal wetland loss and gain were estimated as the proportion of the randomly sampled pixels attributed to the two driver categories.

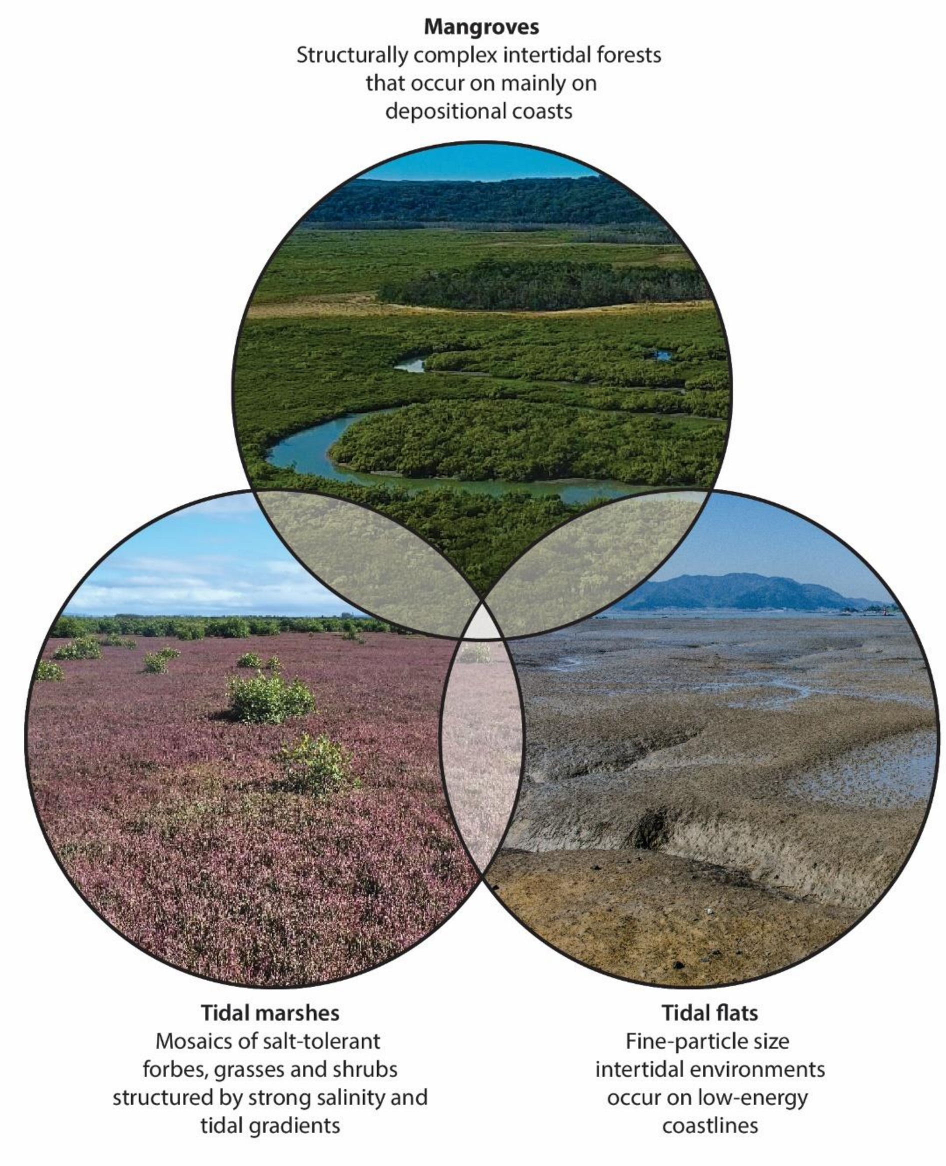

Figure S1.

Representative examples of the three intertidal ecosystem types included in the tidal wetland map class.

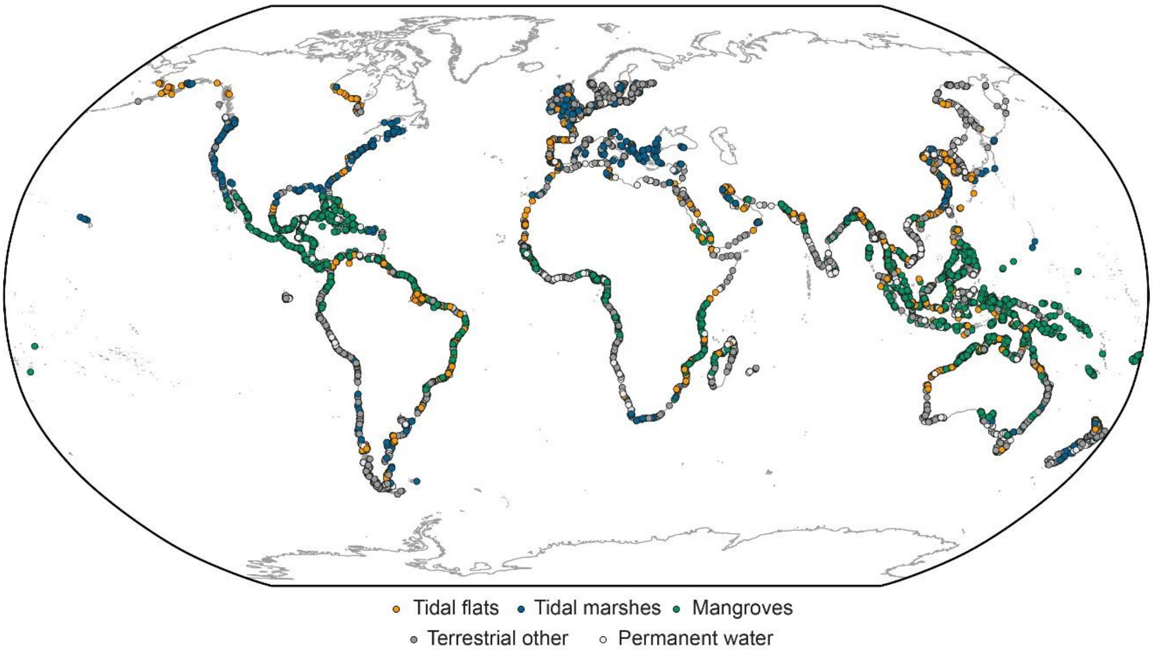

Figure S2.

The global distribution of the training data collected to train the tidal wetlands classification model and classify each pixel to ecosystem type. All training data was collected for the reference period 2014–2016.

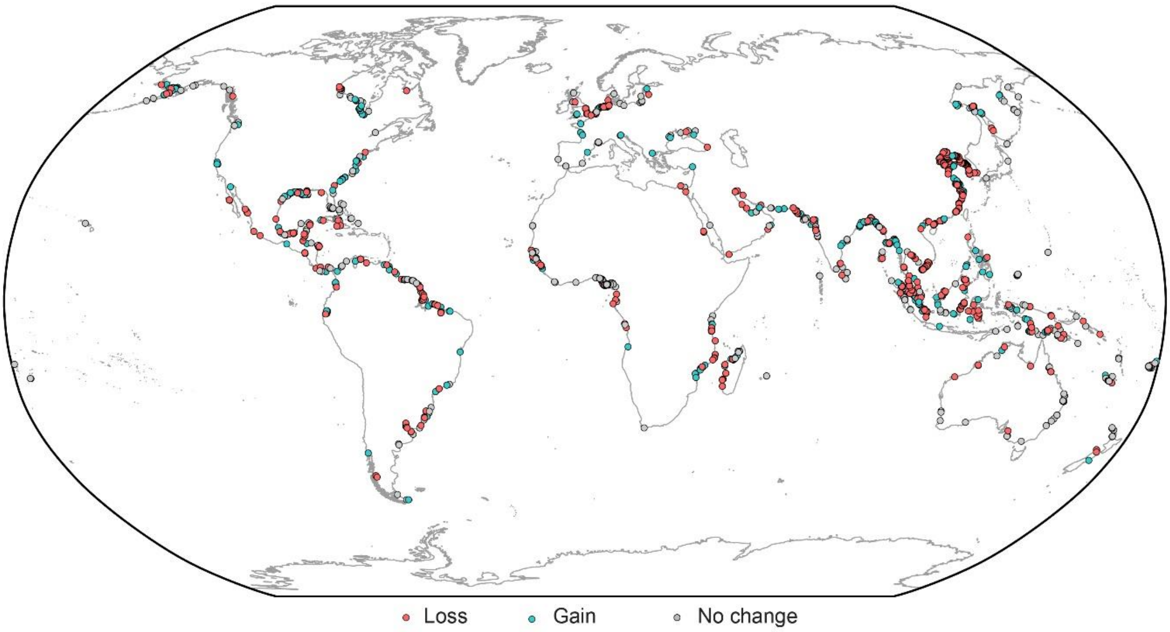

Figure S3.
The global distribution of the training data (n = 1,727) collected to train the global tidal wetland change model for the period 1999–2019.

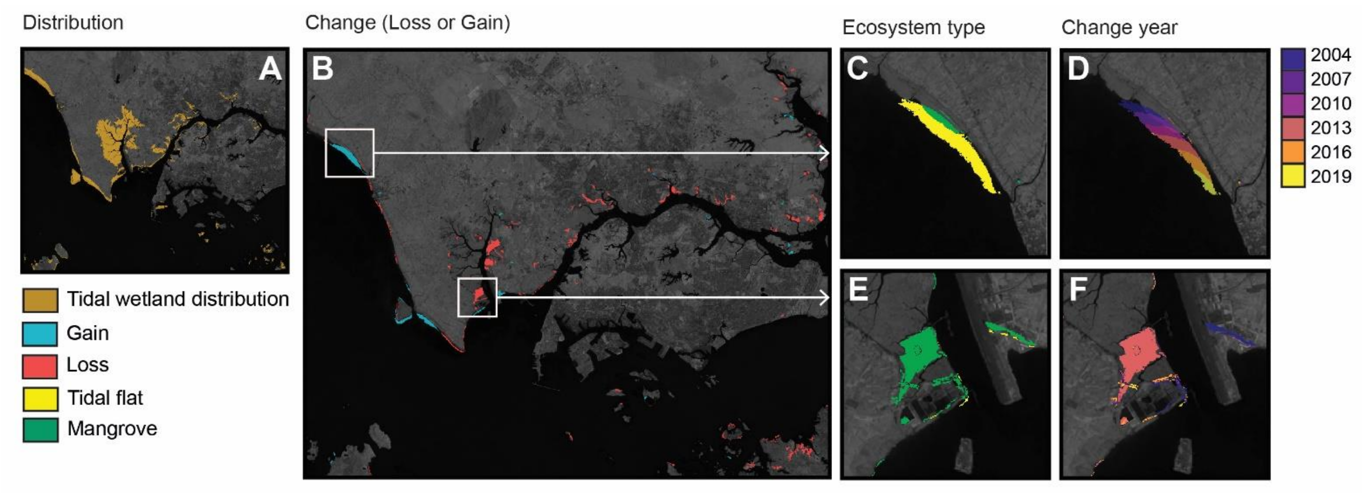

Figure S4.

Example of change detected in tidal wetlands from 1999 to 2019. The figure shows (**A**) the distribution of tidal wetlands (tidal flat, tidal marsh or mangrove) in Malaysia and Singapore, centered at approximately 1.4°N, 103.6°E; (**B**) the loss (red) and gain (blue) data layers. The detailed insets show a new area of tidal wetland caused by sediment deposition, by gain type (**C**) and gain year (**D**); and (**E**) detailed inset of loss by deforestation for an industrial port development, showing loss type (**E**) and loss year (**F**).

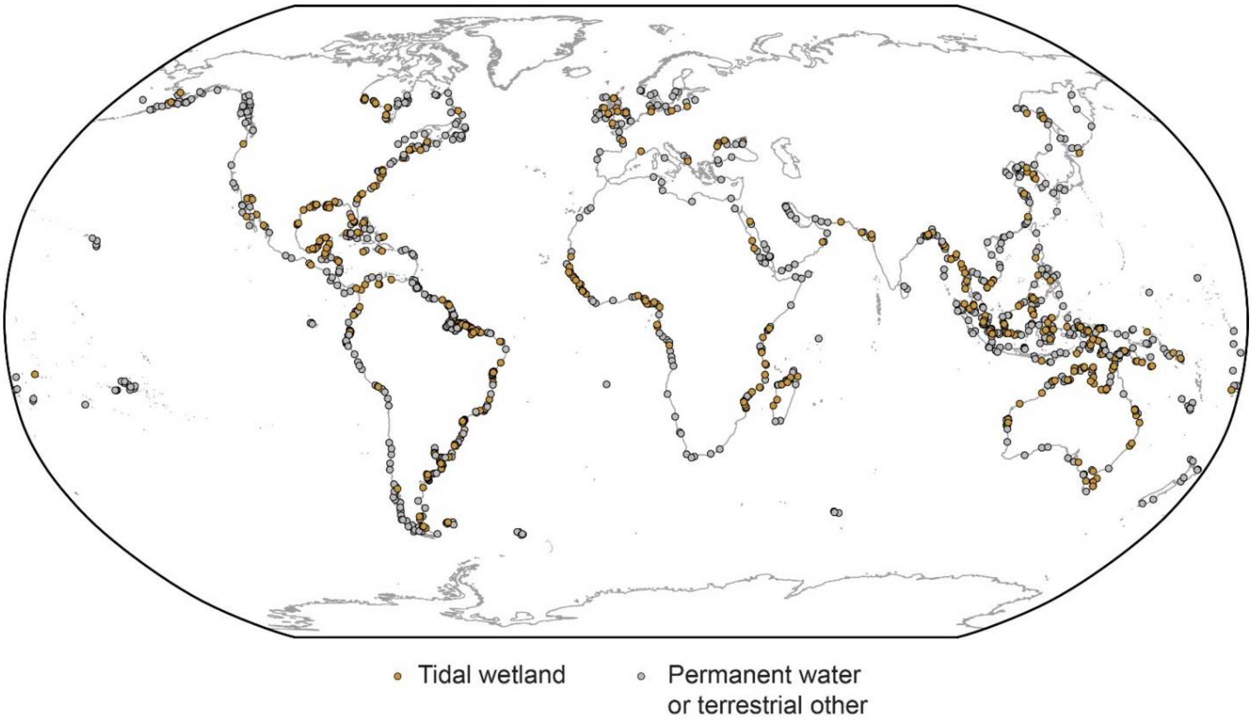

Figure S5.
The validation samples (n = 1359) used to assess the accuracy of the tidal wetland extent product.

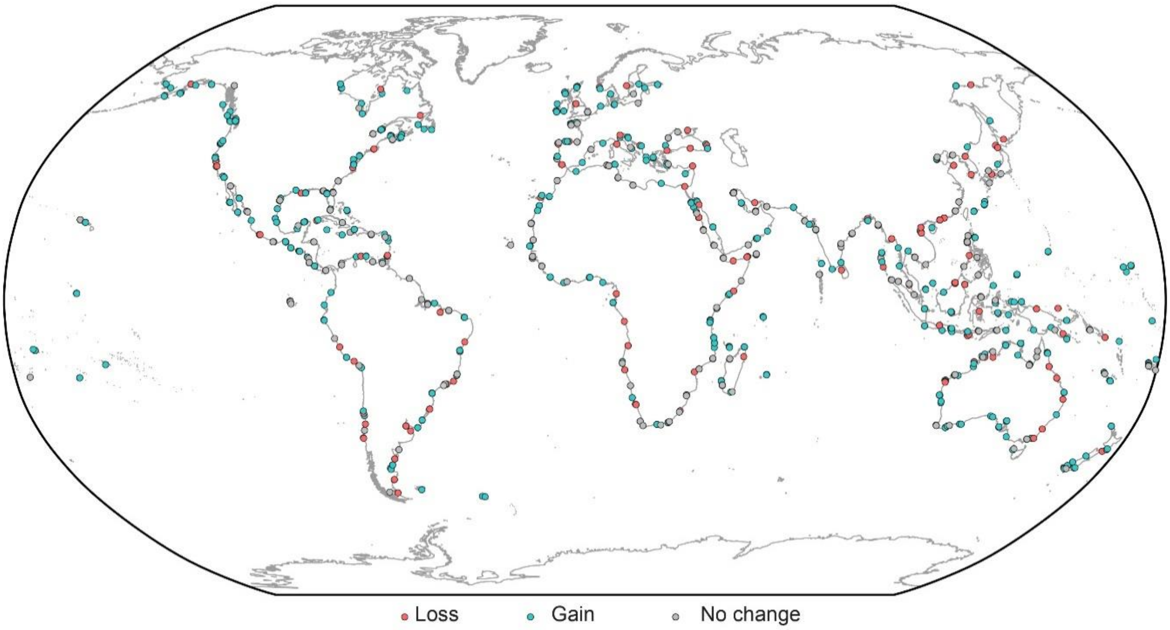

Figure S6.

The validation samples (n = 3060) used to assess the accuracy of the global tidal wetland change product.

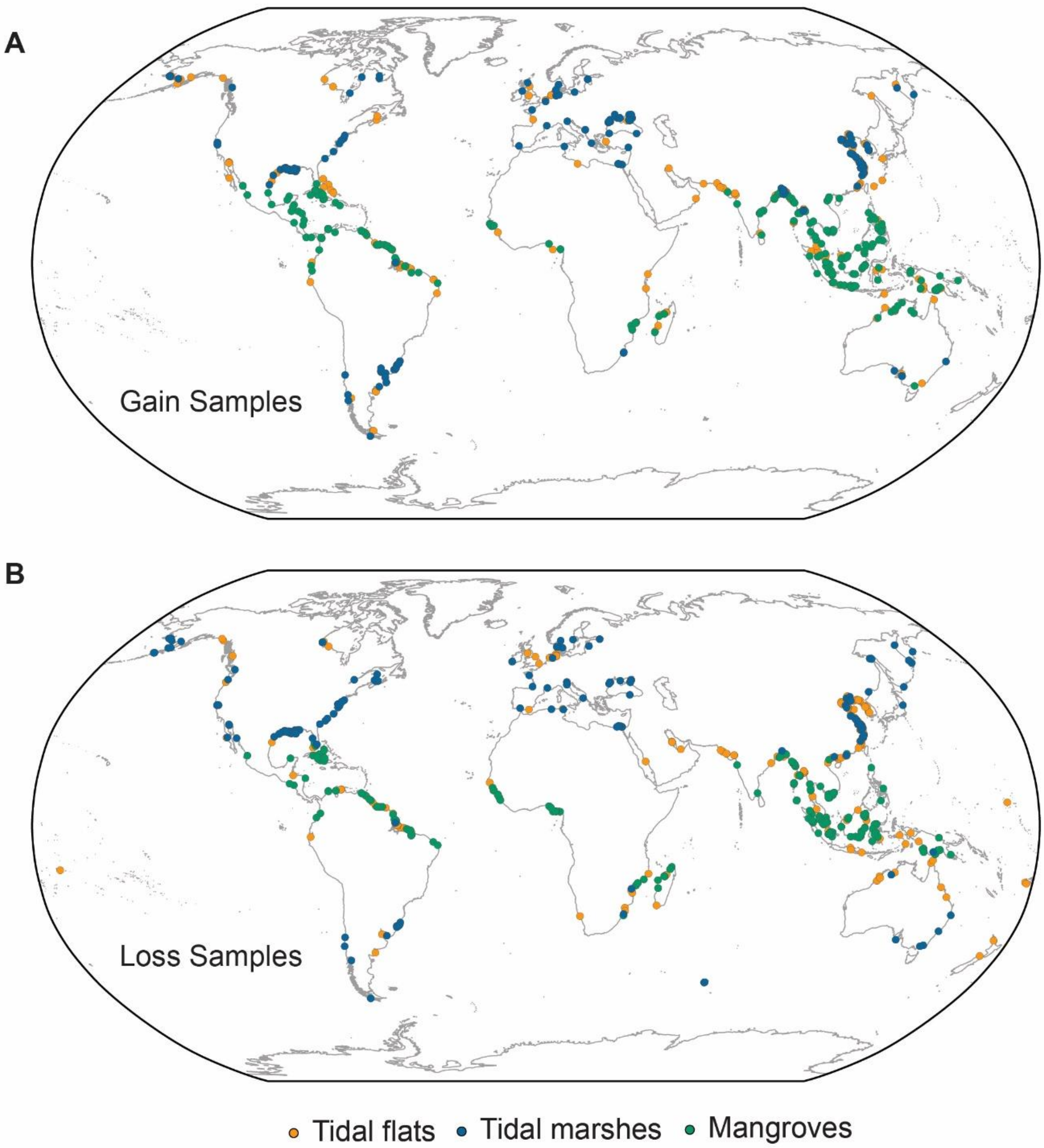

Figure S7.

The driver annotation samples used to assess the relative contribution of direct versus indirect drivers on observed losses and gains of tidal wetlands (n = 1500). The figure shows samples of observed change stratified by ecosystem type for tidal wetland gains (A) and losses (B).

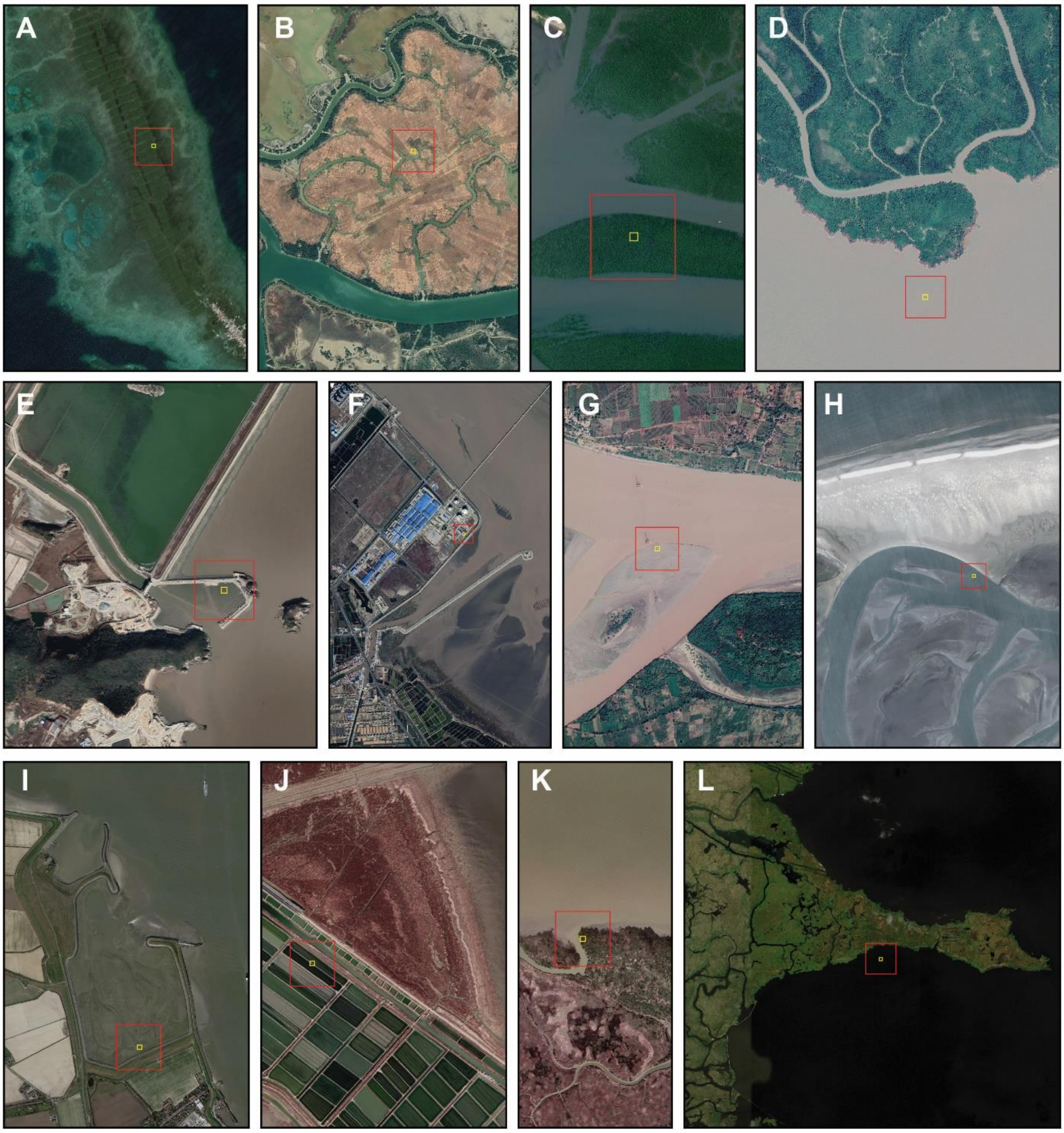

Figure S8.

Examples of direct and indirect drivers of tidal wetland loss and gain. Each row of images from Google Earth Pro indicates an intertidal ecosystem type (mangrove, top; tidal flat, middle; tidal marsh, bottom) and column by direct gain (A, E, I), direct loss (B, F, J), indirect gain (C, G, K) and indirect loss (D, H, L). Yellow squares are 30 x 30-m pixels used to annotate driver type and red squares are 300 x 300-m scale references.

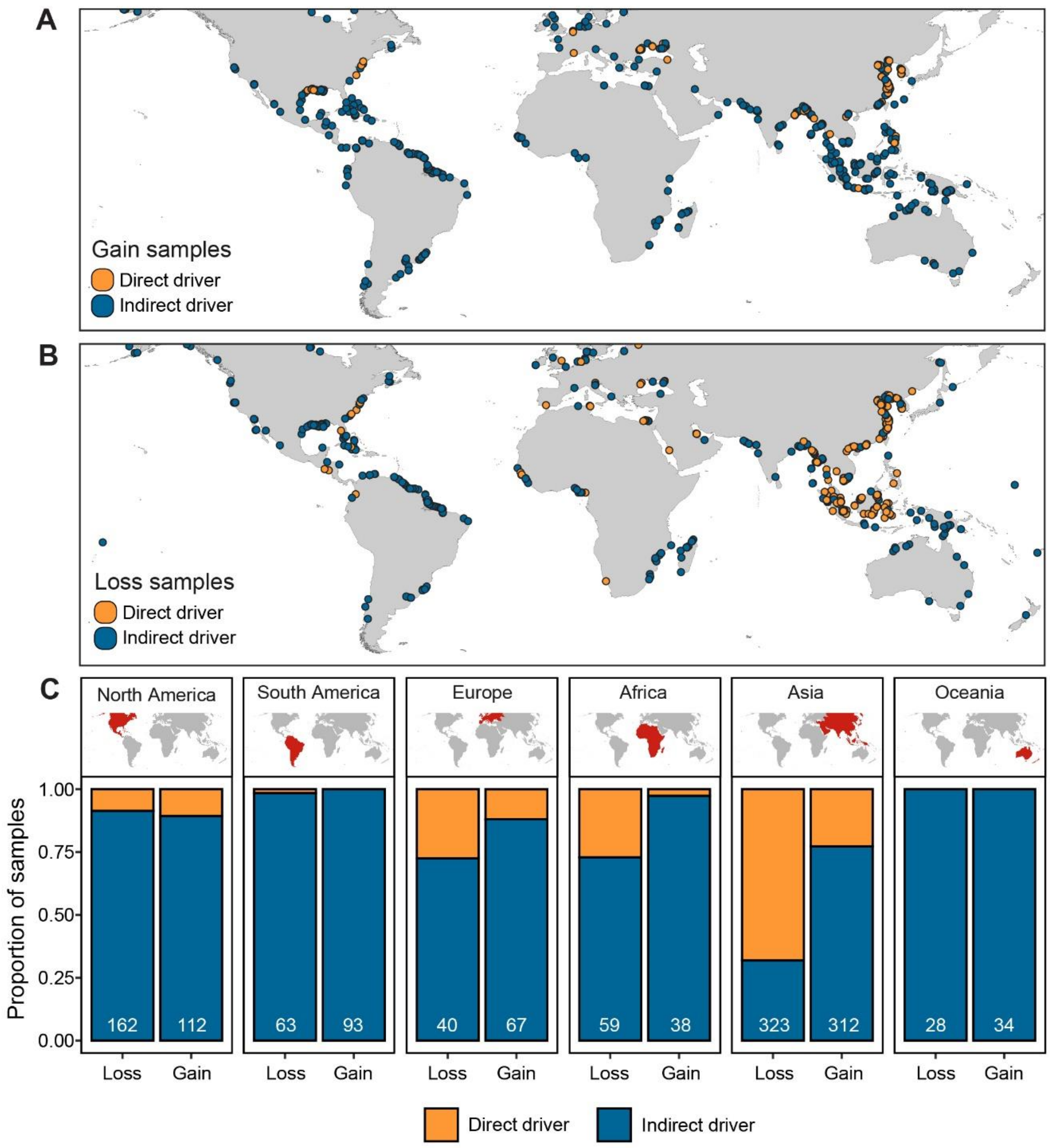

Figure S9.

The contribution of direct and indirect drivers to the observed tidal wetland change. The distribution of the weighted samples used in image interpretation to annotate drivers of gain (A) and loss (B). (C) The proportion of samples attributed to direct and indirect losses per continent. Numbers in each bar indicate the number of samples from the weighted probability sample used to attribute drivers of change.

Table S1.

Datasets used in the global intertidal extent classification models. Each random forest model used per-pixel information from these covariate layers to classify each pixel as tidal wetland or not and change pixels as mangrove, tidal marsh or tidal flats. Four variables in the classification models were static across all years of the time series (elevation, slope, aspect and latitude).

Raw Input Data	**Variables**	**Reducers applied per 3-year period**	**No. covariate layers per time period**	**Produced for each time period**	**Source (web link)**
ALOS World 3D - 30m version 2.2 (AW3D30)	Aspect Elevation Slope	N/A	3	No	JAXA[1]
Landsat Collection-1 At-Surface Reflectance	Automated Water Extraction Index (AWEI) Enhanced Vegetation Index (EVI) Modified Normalized Difference Water Index (MNDWI) Normalized Difference Water Index (NDVI) Normalized Difference Water Index (NDWI)	Minimum Maximum Standard Deviation Median 10th Percentile 25th Percentile 50th Percentile 75th Percentile 90th Percentile 0–10 Interval Mean 10–25 Interval Mean 25–50 Interval Mean 50–75 Interval Mean 75–90 Interval Mean 90–100 Interval Mean 10–90 Interval Mean 25–75 Interval Mean	85	Yes	USGS[2]
	Green band Near Infrared band (NIR) Short-wave Infrared band (SWIR)	10–90 Interval Mean	3	Yes	USGS[2]
Latitude	Latitude	N/A	1	No	Developed by authors in Earth Engine
Minimum Temperature (ERA5 ECMWF)	Minimum Temperature	Minimum	1	Yes	Copernicus Climate Data Store[3]

[1] http://www.eorc.jaxa.jp/ALOS/en/aw3d30/
[2] https://www.usgs.gov/media/files/landsat-collection-1-level-1-product-definition
[3] https://cds.climate.copernicus.eu/cdsapp#!/dataset/reanalysis-era5-single-levels

Table S2.
Covariate data inputs used in the tidal wetland change random forest classification model.

Raw Input Data	Variables	Reducers applied per 3-year period	Processing for change analysis	No. covariate layers in intertidal ecosystem change classification model
Linear trend of tidal wetland probability layers (representing agreement among random forest trees for binary tidal wetland class)	Random forest probability layer of tidal wetland extent (result of Stage 1 analysis)	N/A	Per-pixel linear model of 7 time-series random forest probability layers	1
Landsat Collection-1 At-Surface Reflectance	Automated Water Extraction Index (AWEI) Enhanced Vegetation Index (EVI) Modified Normalized Difference Water Index (MNDWI) Normalized Difference Water Index (NDVI) Normalized Difference Water Index (NDWI)	Minimum Maximum Standard Deviation Median 10th Percentile 25th Percentile 50th Percentile 75th Percentile 90th Percentile 0–10 Interval Mean 10–25 Interval Mean 25–50 Interval Mean 50–75 Interval Mean 75–90 Interval Mean 90–100 Interval Mean 10–90 Interval Mean 25–75 Interval Mean	Difference between 1999-2001 and 2017-2019 pixel values	85
	Green band Near Infrared band (NIR)	10–90 Interval Mean	Difference between 1999-2001	3

	Short-wave Infrared band (SWIR)		and 2017-2019 pixel values	

Table S3.

Global, continental and national summaries of tidal wetland loss and gain between 1999 and 2019. Note that only countries that contribute ≥ 0.1% of global net change are included in this table.

Unit	Loss area (km^2)	Gain area (km^2)	Net change (km^2)	Total tidal wetland change area (km^2)	Contribution to global net change (%)	Loss to Gain Ratio
GLOBAL	-13656	9698	-3958	23355	100	1.4
ASIA	-7836	4905	-2931	12741	74.1	1.6
NORTH AMERICA	-1512	1103	-409	2615	10.3	1.4
AFRICA	-1075	684	-390	1759	9.9	1.6
SOUTH AMERICA	-1777	1493	-284	3269	7.2	1.2
OCEANIA	-720	563	-157	1283	4	1.3
EUROPE	-737	951	214	1688	-5.4	0.8
Indonesia, Republic of	-2198	772	-1426	2970	36	2.9
China, People's Republic of	-2246	1433	-813	3679	20.6	1.6
Myanmar, Union of	-896	421	-475	1317	12	2.1
Brazil, Federative Republic of	-1140	828	-312	1969	7.9	1.4
Vietnam, Socialist Republic of	-347	144	-203	490	5.1	2.4
Cuba, Republic of	-264	70	-193	334	4.9	3.8
United States of America	-843	668	-174	1511	4.4	1.3
Nigeria, Federal Republic of	-185	27	-158	212	4	6.9
Malaysia	-290	148	-142	437	3.6	2
Guinea, Republic of	-93	22	-70	115	1.8	4.1
Papua New Guinea, Independent State of	-214	148	-66	363	1.7	1.4
Korea, Democratic People's Republic of	-129	79	-50	208	1.3	1.6
Guyana, Co-operative Republic of	-92	45	-47	137	1.2	2
Marshall Islands, Republic of the	-42	1	-41	43	1	41.8
Bahamas, Commonwealth of the	-67	32	-35	99	0.9	2.1
Ghana, Republic of	-34	3	-32	37	0.8	13
Saudi Arabia, Kingdom of	-36	7	-29	43	0.7	4.8
Mozambique, Republic of	-202	176	-26	378	0.7	1.1
Thailand, Kingdom of	-89	64	-24	153	0.6	1.4
Guinea-Bissau, Republic of	-85	61	-24	146	0.6	1.4
Australia, Commonwealth of	-380	357	-23	737	0.6	1.1
Colombia, Republic of	-135	113	-22	249	0.6	1.2
Qatar, State of	-22	1	-22	23	0.5	38.6
Sierra Leone, Republic of	-22	2	-20	24	0.5	8.9
Madagascar, Republic of	-217	198	-19	414	0.5	1.1
Pakistan, Islamic Republic of	-97	79	-18	176	0.5	1.2

New Zealand	-47	30	-17	76	0.4	1.6
Nicaragua, Republic of	-34	19	-15	54	0.4	1.8
Egypt, Arab Republic of	-77	63	-13	140	0.3	1.2
Tunisia, Tunisian Republic	-20	7	-13	27	0.3	2.7
South Africa, Republic of	-32	21	-11	53	0.3	1.6
Cambodia, Kingdom of	-16	6	-10	22	0.3	2.6
Bahrain, Kingdom of	-9	0	-9	9	0.2	25.2
Honduras, Republic of	-24	15	-8	39	0.2	1.5
Samoa, Independent State of	-7	0	-7	8	0.2	33
Peru, Republic of	-20	14	-7	34	0.2	1.5
Somalia, Somali Republic	-7	2	-6	9	0.1	4.8
Italy, Italian Republic	-20	14	-6	34	0.1	1.4
Brunei Darussalam	-6	1	-5	7	0.1	8.2
Fiji, Republic of the Fiji Islands	-13	7	-5	20	0.1	1.7
Gabon, Gabonese Republic	-9	4	-5	13	0.1	2
Belize	-11	7	-4	18	0.1	1.7
Jamaica	-6	2	-4	8	0.1	2.6
Sweden, Kingdom of	-5	1	-4	6	0.1	4.1
Cameroon, Republic of	-12	9	-4	21	0.1	1.4
Liberia, Republic of	-4	1	-3	4	0.1	6.7
Iraq, Republic of	-5	2	-3	7	0.1	2.3
Haiti, Republic of	-10	7	-3	17	0.1	1.4
Dominican Republic	-6	8	2	13	-0.1	0.7
Trinidad and Tobago, Republic of	-1	4	2	5	-0.1	0.4
Libyan Arab Jamahiriya	-3	5	2	8	-0.1	0.6
Kiribati, Republic of	0	3	2	3	-0.1	0.2
Ireland	-11	14	2	25	-0.1	0.8
Japan	-25	28	3	53	-0.1	0.9
Mauritania, Islamic Republic of	-1	4	3	6	-0.1	0.3
Taiwan	-7	10	3	17	-0.1	0.7
Turkey, Republic of	-31	34	3	65	-0.1	0.9
Montenegro, Republic of	-1	5	3	6	-0.1	0.3
Costa Rica, Republic of	-10	13	4	23	-0.1	0.7
Mexico, United Mexican States	-205	210	4	415	-0.1	1
Ecuador, Republic of	-34	39	6	73	-0.1	0.9
Kuwait, State of	-6	14	7	20	-0.2	0.5
Cyprus, Republic of	0	9	8	9	-0.2	0
France, French Republic	-168	178	9	346	-0.2	0.9
Korea, Republic of	-121	133	12	255	-0.3	0.9
Tanzania, United Republic of	-27	40	13	67	-0.3	0.7
Netherlands, Kingdom of the	-61	75	14	136	-0.4	0.8
Panama, Republic of	-21	38	16	59	-0.4	0.6
United Kingdom of Great Britain & Northern Ireland	-124	146	22	270	-0.6	0.8
Venezuela, Bolivarian Republic of	-129	154	25	282	-0.6	0.8

Romania	-6	31	25	38	-0.6	0.2
Ukraine	-25	51	27	76	-0.7	0.5
Suriname, Republic of	-101	135	35	236	-0.9	0.7
Argentina, Argentine Republic	-89	125	37	214	-0.9	0.7
Russian Federation	-225	274	49	500	-1.2	0.8
Germany, Federal Republic of	-120	212	92	332	-2.3	0.6
Bangladesh, People's Republic of	-595	709	114	1304	-2.9	0.8
Philippines, Republic of the	-80	208	128	287	-3.2	0.4

Table S4.
Summary of tidal wetland pixels that transitioned from one intertidal ecosystem type to another between 1999 and 2019.

Transition Type	**Area (km^2)**	**Percent of total transition area (%)**
Tidal marsh to tidal flat	643.0	9.7
Tidal marsh to mangrove	910.3	13.7
Tidal flat to tidal marsh	1902.1	28.6
Tidal flat to mangrove	1779.4	26.7
Mangrove to tidal flat	552.2	8.3
Mangrove to tidal marsh	865.2	13.0
Total transition pixels	**6652.3**	**100.0**

Table S5.

Class accuracy results for the global tidal wetland classification model based on validation sample points over the mapped area (n = 1359).

		Reference	
		Other	**Tidal wetland**
Mapped	**Other**	673	8
	Tidal wetland	191	487

Table S6.

Quantitative accuracy assessment results for the global tidal wetland classification model based on validation sample points over the mapped area (n = 1359). Quantitative accuracy assessments involved bootstrapping the validation samples (n = 1000 iterations), with the mean of the sampling distribution as the reported accuracy estimate and the 0.025 and 0.975 percentiles of the sampling distribution as the 95% confidence interval.

Error	**Estimate**	**95% Confidence Interval**	
		Lower	**Upper**
Overall accuracy	0.854	0.836	0.871
Other (commission)	0.988	0.979	0.996
Other (omission)	0.779	0.758	0.801
Tidal wetland (commission)	0.719	0.684	0.754
Tidal wetland (omission)	0.984	0.972	0.994

Table S7.

Class accuracy results for the global intertidal change classification model based on validation sample points over the mapped area (n = 3059).

		Reference		
		Loss	Stable	Gain
Mapped	Loss	143	65	11
	Stable	26	477	107
	Gain	6	57	86

Table S8.

Quantitative accuracy assessment results for the global intertidal change classification model based on validation sample points over the mapped area (n = 3059). Quantitative accuracy assessments involved bootstrapping the validation samples (n = 1000 iterations), with the mean of the sampling distribution as the reported accuracy estimate and the 0.025 and 0.975 percentiles of the sampling distribution as the 95% confidence interval.

Error	**Estimate**	**95% Confidence Interval**	
		Lower	**Upper**
Overall accuracy	0.722	0.696	0.751
Loss (commission)	0.652	0.589	0.712
Loss (omission)	0.817	0.766	0.871
No change (commission)	0.782	0.748	0.815
No change (omission)	0.796	0.773	0.820
Gain (commission)	0.579	0.503	0.658
Gain (omission)	0.423	0.374	0.473

Table S9.

The proportion of observed tidal wetland changes attributed to direct drivers at the 30-m pixel scale. Each random sample of tidal wetland change was assessed using high-resolution time-series images available in Google Earth Pro. Direct drivers included changes due to land changes such as aquaculture, agriculture, plantations, urban and industrial development, and other artificial objects such as coastal infrastructure (bridges and dikes). Indirect drivers of change were not directly observable in high-resolution time-series images and include the effects of natural coastal processes, climate change, and remote drivers of change such as change in catchment sediment flux. Samples that could not be allocated to a direct or indirect driver due to lack of high-resolution imagery or uncertainty about tidal wetland change were excluded from the analysis.

Change type	No. Direct	No. Indirect	SE	Direct (%)	n (sampled)	n (excluded)	n (annotated)
Mangrove gain	17	208	3.964	8	250	25	225
Mangrove loss	110	110	7.416	50	250	30	220
Tidal marsh gain	68	155	6.875	30	250	27	223
Tidal marsh loss	47	169	6.064	22	250	34	216
Tidal flat gain	7	201	2.601	3	250	42	208
Tidal flat loss	105	134	7.673	44	250	11	239
Tidal Wetland Gain	92	564	8.894	14	750	94	656
Tidal wetland loss	262	413	12.661	39	750	75	675

Table S10.

Attribution of observed changes to direct or indirect drivers by continent. The contribution of direct and indirect drivers was estimated as the proportion of a global weighted probability sample of observed changes to the direct driver class (% direct).

Continent	Tidal wetland		Mangrove		Tidal marsh		Tidal flats	
	Loss (% direct)	Gain (% direct)	Loss (% direct)	Gain (% direct)	Loss (% direct)	Gain (% direct)	Loss (% direct)	Gain (% direct)
Africa	27	3	20	5	50	0	15	0
Asia	68	23	75	13	69	59	62	5
Europe	28	12	0	0	38	17	7	5
North America	9	11	18	0	8	19	0	4
Oceania	0	0	0	0	0	0	0	0
South America	2	0	3	0	0	0	0	0

References and Notes

<jrn>1. E. B. Barbier, S. D. Hacker, C. Kennedy, E. W. Koch, A. C. Stier, B. R. Silliman, The value of estuarine and coastal ecosystem services. *Ecol. Monogr.* **81**, 169–193 (2011). doi:10.1890/10-1510.1</jrn>

<jrn>2. M. D. Spalding, A. L. McIvor, M. W. Beck, E. W. Koch, I. Möller, D. J. Reed, P. Rubinoff, T. Spencer, T. J. Tolhurst, T. V. Wamsley, B. K. Wesenbeeck, E. Wolanski, C. D. Woodroffe, Coastal ecosystems: A critical element of risk reduction. *Conserv. Lett.* **7**, 293–301 (2014). doi:10.1111/conl.12074</jrn>

<jrn>3. E. B. Barbier, Disaster Management. A global strategy for protecting vulnerable coastal populations. *Science* **345**, 1250–1251 (2014). doi:10.1126/science.1254629 Medline</jrn>

<jrn>4. D. A. Friess, K. Rogers, C. E. Lovelock, K. W. Krauss, S. E. Hamilton, S. Y. Lee, R. Lucas, J. Primavera, A. Rajkaran, S. Shi, The state of the world's mangrove forests: Past, present, and future. *Annu. Rev. Environ. Resour.* **44**, 89–115 (2019). doi:10.1146/annurev-environ-101718-033302</jrn>

<jrn>5. D. M. FitzGerald, Z. Hughes, Marsh Processes and Their Response to Climate Change and Sea-Level Rise. *Annu. Rev. Earth Planet. Sci.* **47**, 481–517 (2019). doi:10.1146/annurev-earth-082517-010255</jrn>

<jrn>6. C. E. Lovelock, D. R. Cahoon, D. A. Friess, G. R. Guntenspergen, K. W. Krauss, R. Reef, K. Rogers, M. L. Saunders, F. Sidik, A. Swales, N. Saintilan, X. Thuyen, T. Triet, The vulnerability of Indo-Pacific mangrove forests to sea-level rise. *Nature* **526**, 559–563 (2015). doi:10.1038/nature15538 Medline</jrn>

<eref>7. S. Fagherazzi, M. L. Kirwan, S. M. Mudd, G. R. Guntenspergen, S. Temmerman, A. D'Alpaos, J. van de Koppel, J. M. Rybczyk, E. Reyes, C. Craft, J. Clough, Numerical models of salt marsh evolution: Ecological, geomorphic, and climatic factors. *Rev. Geophys.* **50**, RG1002 (2012). doi:10.1029/2011RG000359</eref>

<jrn>8. M. L. Kirwan, J. P. Megonigal, Tidal wetland stability in the face of human impacts and sea-level rise. *Nature* **504**, 53–60 (2013). doi:10.1038/nature12856 Medline</jrn>

<jrn>9. N. J. Murray, S. R. Phinn, M. DeWitt, R. Ferrari, R. Johnston, M. B. Lyons, N. Clinton, D. Thau, R. A. Fuller, The global distribution and trajectory of tidal flats. *Nature* **565**, 222–225 (2019). doi:10.1038/s41586-018-0805-8 Medline</jrn>

<jrn>10. E. Bayraktarov, M. I. Saunders, S. Abdullah, M. Mills, J. Beher, H. P. Possingham, P. J. Mumby, C. E. Lovelock, The cost and feasibility of marine coastal restoration. *Ecol. Appl.* **26**, 1055–1074 (2016). doi:10.1890/15-1077 Medline</jrn>

<jrn>11. M. L. Kirwan, S. Temmerman, E. E. Skeehan, G. R. Guntenspergen, S. Fagherazzi, Overestimation of marsh vulnerability to sea level rise. *Nat. Clim. Chang.* **6**, 253–260 (2016). doi:10.1038/nclimate2909</jrn>

<jrn>12. M. Schuerch, T. Spencer, S. Temmerman, M. L. Kirwan, C. Wolff, D. Lincke, C. J. McOwen, M. D. Pickering, R. Reef, A. T. Vafeidis, J. Hinkel, R. J. Nicholls, S. Brown, Future response of global coastal wetlands to sea-level rise. *Nature* **561**, 231–234 (2018). doi:10.1038/s41586-018-0476-5 Medline</jrn>

<jrn>13. P. Bunting, A. Rosenqvist, R. Lucas, L.-M. Rebelo, L. Hilarides, N. Thomas, A. Hardy, T. Itoh, M. Shimada, C. Finlayson, The Global Mangrove Watch—A new 2010 global baseline of mangrove extent. *Remote Sens.* **10**, 1669 (2018). doi:10.3390/rs10101669</jrn>

<jrn>14. L. Goldberg, D. Lagomasino, N. Thomas, T. Fatoyinbo, Global declines in human-driven mangrove loss. *Glob. Change Biol.* **26**, 5844–5855 (2020). doi:10.1111/gcb.15275 Medline</jrn>

<jrn>15. C. J. Mcowen, L. V. Weatherdon, J. V. Bochove, E. Sullivan, S. Blyth, C. Zockler, D. Stanwell-Smith, N. Kingston, C. S. Martin, M. Spalding, S. Fletcher, A global map of saltmarshes. *Biodivers. Data J.* **5**, e11764 (2017). doi:10.3897/BDJ.5.e11764 Medline</jrn>

<foot>16. Materials and methods are available as supplementary materials.</foot>

<jrn>17. P. I. Macreadie, A. Anton, J. A. Raven, N. Beaumont, R. M. Connolly, D. A. Friess, J. J. Kelleway, H. Kennedy, T. Kuwae, P. S. Lavery, C. E. Lovelock, D. A. Smale, E. T. Apostolaki, T. B. Atwood, J. Baldock, T. S. Bianchi, G. L. Chmura, B. D. Eyre, J. W. Fourqurean, J. M. Hall-Spencer, M. Huxham, I. E. Hendriks, D. Krause-Jensen, D. Laffoley, T. Luisetti, N. Marbà, P. Masque, K. J. McGlathery, J. P. Megonigal, D. Murdiyarso, B. D. Russell, R. Santos, O. Serrano, B. R. Silliman, K. Watanabe, C. M. Duarte, The future of Blue Carbon science. *Nat. Commun.* **10**, 3998 (2019). doi:10.1038/s41467-019-11693-w Medline</jrn>

<edb>18. M. Spalding, M. Leal, Eds., "The state of the world's mangroves 2021" (Global Mangrove Alliance, 2021).</edb>

<jrn>19. J. H. Nienhuis, A. D. Ashton, D. A. Edmonds, A. J. F. Hoitink, A. J. Kettner, J. C. Rowland, T. E. Törnqvist, Global-scale human impact on delta morphology has led to net land area gain. *Nature* **577**, 514–518 (2020). doi:10.1038/s41586-019-1905-9 Medline</jrn>

<jrn>20. K. B. Gedan, B. R. Silliman, M. D. Bertness, Centuries of human-driven change in salt marsh ecosystems. *Annu. Rev. Mar. Sci.* **1**, 117–141 (2009). doi:10.1146/annurev.marine.010908.163930 Medline</jrn>

<jrn>21. J. P. M. Syvitski, A. J. Kettner, I. Overeem, E. W. H. Hutton, M. T. Hannon, G. R. Brakenridge, J. Day, C. Vörösmarty, Y. Saito, L. Giosan, R. J. Nicholls, Sinking deltas due to human activities. *Nat. Geosci.* **2**, 681–686 (2009). doi:10.1038/ngeo629</jrn>

<jrn>22. D. Lagomasino, T. Fatoyinbo, E. Castañeda-Moya, B. D. Cook, P. M. Montesano, C. S. R. Neigh, L. A. Corp, L. E. Ott, S. Chavez, D. C. Morton, Storm surge and ponding explain mangrove dieback in southwest Florida following Hurricane Irma. *Nat. Commun.* **12**, 4003 (2021). doi:10.1038/s41467-021-24253-y Medline</jrn>

<jrn>23. L. A. Deegan, D. S. Johnson, R. S. Warren, B. J. Peterson, J. W. Fleeger, S. Fagherazzi, W. M. Wollheim, Coastal eutrophication as a driver of salt marsh loss. *Nature* **490**, 388–392 (2012). doi:10.1038/nature11533 Medline</jrn>

<jrn>24. X. Wang, X. Xiao, X. Xu, Z. Zou, B. Chen, Y. Qin, X. Zhang, J. Dong, D. Liu, L. Pan, B. Li, Rebound in China's coastal wetlands following conservation and restoration. *Nat. Sustain.* **4**, 1076–1083 (2021). doi:10.1038/s41893-021-00793-5</jrn>

<jrn>25. M. Liu, D. Mao, Z. Wang, L. Li, W. Man, M. Jia, C. Ren, Y. Zhang, Rapid invasion of *Spartina alterniflora* in the coastal zone of mainland China: New observations from Landsat OLI images. *Remote Sens.* **10**, 1933 (2018). doi:10.3390/rs10121933</jrn>

<jrn>26. X.-P. Song, M. C. Hansen, S. V. Stehman, P. V. Potapov, A. Tyukavina, E. F. Vermote, J. R. Townshend, Global land change from 1982 to 2016. *Nature* **560**, 639–643 (2018). doi:10.1038/s41586-018-0411-9 Medline</jrn>

<jrn>27. C. M. Duarte, S. Agusti, E. Barbier, G. L. Britten, J. C. Castilla, J.-P. Gattuso, R. W. Fulweiler, T. P. Hughes, N. Knowlton, C. E. Lovelock, H. K. Lotze, M. Predragovic, E. Poloczanska, C. Roberts, B. Worm, Rebuilding marine life. *Nature* **580**, 39–51 (2020). doi:10.1038/s41586-020-2146-7 Medline</jrn>

<jrn>28. K. C. Cavanaugh, E. M. Dangremond, C. L. Doughty, A. P. Williams, J. D. Parker, M. A. Hayes, W. Rodriguez, I. C. Feller, Climate-driven regime shifts in a mangrove-salt marsh ecotone over the past 250 years. *Proc. Natl. Acad. Sci. U.S.A.* **116**, 21602–21608 (2019). doi:10.1073/pnas.1902181116 Medline</jrn>

<jrn>29. N. Saintilan, N. S. Khan, E. Ashe, J. J. Kelleway, K. Rogers, C. D. Woodroffe, B. P. Horton, Thresholds of mangrove survival under rapid sea level rise. *Science* **368**, 1118–1121 (2020). doi:10.1126/science.aba2656 Medline</jrn>

<jrn>30. P. Nehru, P. Balasubramanian, Mangrove species diversity and composition in the successional habitats of Nicobar Islands, India: A post-tsunami and subsidence scenario. *For. Ecol. Manage.* **427**, 70–77 (2018). doi:10.1016/j.foreco.2018.05.063</jrn>

<eref>31. N. Murray, Code for high-resolution mapping of losses and gains of Earth's tidal wetlands, v0.1.2, Zenodo (2022); https://doi.org/10.5281/zenodo.5968865</eref>

<eref>32. N. Murray, T. A. Worthington, M. Lyons, Intertidal ecosystem training data for mapping Earth's tidal wetlands, Figshare (2018); https://doi.org/10.6084/m9.figshare.19121660</eref>

<eref>33. N. Murray, Data descriptor for Murray global tidal wetland change, v0.1.0, Zenodo (2022); https://doi.org/10.5281/zenodo.6503080</eref>

<jrn>34. S. K. Hong, C.-H. Koh, R. R. Harris, J.-E. Kim, J.-S. Lee, B.-S. Ihm, Land use in Korean tidal wetlands: Impacts and management strategies. *Environ. Manage.* **45**, 1014–1026 (2010). doi:10.1007/s00267-006-0164-3 Medline</jrn>

<edb>35. D. A. Keith, J. R. Ferrer-Paris, E. Nicholson, R. T. Kingsford, in *The IUCN Global Ecosystem Typology 2.0: Descriptive Profiles for Biomes and Ecosystem Functional Groups*, D. A. Keith, J. R. Ferrer-Paris, E. Nicholson, R. T. Kingsford, Eds. (IUCN, 2020); https://doi.org/10.2305/IUCN.CH.2020.13.en.</edb>

<edb>36. M. J. Bishop, N. J. Murray, S. Swearer, D. A. Keith, "MT1.2 Muddy Shorelines" in *The IUCN Global Ecosystem Typology 2.0: Descriptive profiles for biomes and ecosystem functional groups*, D. A. Keith, J. R. Ferrer-Paris, E. Nicholson, R. T. Kingsford, Eds. (IUCN, 2020).</edb>

<edb>37. D. A. Keith, A. H. Altieri, J. Loidi, M. J. Bishop, "MFT1.3 Coastal saltmarshes and reedbeds" in *The IUCN Global Ecosystem Typology 2.0: Descriptive profiles for biomes and ecosystem functional groups*, D. A. Keith, J. R. Ferrer-Paris, E. Nicholson, R. T. Kingsford, Eds. (IUCN, 2020).</edb>

<edb>38. M. J. Bishop, A. H. Altieri, T. S. Bianchi, D. A. Keith, "MFT1.2 Intertidal forests and shrublands" in *The IUCN Global Ecosystem Typology 2.0: Descriptive profiles for biomes and ecosystem functional groups*, D. A. Keith, J. R. Ferrer-Paris, E. Nicholson, R. T. Kingsford, Eds. (IUCN, 2020).</edb>

<jrn>39. L. Breiman, Random forests. *Mach. Learn.* **45**, 5–32 (2001). doi:10.1023/A:1010933404324</jrn>

<bok>40. US Department of Commerce, C. Amante, B. W. Eakins, "ETOPO1 1 arc-minute global relief model: procedures, data sources and analysis" (NOAA, 2009).</bok>

<jrn>41. T. A. Worthington, P. S. E. zu Ermgassen, D. A. Friess, K. W. Krauss, C. E. Lovelock, J. Thorley, R. Tingey, C. D. Woodroffe, P. Bunting, N. Cormier, D. Lagomasino, R. Lucas, N. J. Murray, W. J. Sutherland, M. Spalding, A global biophysical typology of mangroves and its relevance for ecosystem structure and deforestation. *Sci. Rep.* **10**, 14652 (2020). doi:10.1038/s41598-020-71194-5 Medline</jrn>

<jrn>42. C. Giri, E. Ochieng, L. L. Tieszen, Z. Zhu, A. Singh, T. Loveland, J. Masek, N. Duke, Status and distribution of mangrove forests of the world using earth observation satellite data. *Glob. Ecol. Biogeogr.* **20**, 154–159 (2011). doi:10.1111/j.1466-8238.2010.00584.x</jrn>

<eref>43. N. Earth, Coastline (2020); https://www.naturalearthdata.com/downloads/10m-physical-vectors/10m-coastline.</eref>

<jrn>44. N. Gorelick, M. Hancher, M. Dixon, S. Ilyushchenko, D. Thau, R. Moore, Google Earth Engine: Planetary-scale geospatial analysis for everyone. *Remote Sens. Environ.* **202**, 18–27 (2017). doi:10.1016/j.rse.2017.06.031</jrn>

<eref>45. R Core Team, R: A language and environment for statistical computing (R Foundation for Statistical Computing, 2020); www.R-project.org/.</eref>

<jrn>46. M. C. Hansen, T. R. Loveland, A review of large area monitoring of land cover change using Landsat data. *Remote Sens. Environ.* **122**, 66–74 (2012). doi:10.1016/j.rse.2011.08.024</jrn>

<jrn>47. R. E. Kennedy, S. Andréfouët, W. B. Cohen, C. Gómez, P. Griffiths, M. Hais, S. P. Healey, E. H. Helmer, P. Hostert, M. B. Lyons, G. W. Meigs, D. Pflugmacher, S. R. Phinn, S. L. Powell, P. Scarth, S. Sen, T. A. Schroeder, A. Schneider, R. Sonnenschein, J. E. Vogelmann, M. A. Wulder, Z. Zhu, Bringing an ecological view of change to Landsat-based remote sensing. *Front. Ecol. Environ.* **12**, 339–346 (2014). doi:10.1890/130066</jrn>

<jrn>48. N. J. Murray, D. A. Keith, L. M. Bland, R. Ferrari, M. B. Lyons, R. Lucas, N. Pettorelli, E. Nicholson, The role of satellite remote sensing in structured ecosystem risk assessments. *Sci. Total Environ.* **619–620**, 249–257 (2018). doi:10.1016/j.scitotenv.2017.11.034 Medline</jrn>

<bok>49. US Geological Survey, *Landsat 4-7 Collection 1 (C1) Surface Reflectance (LEDAPS) Product Guide. Version 3.0* (USGS, 2020).</bok>

<jrn>50. P. V. Potapov, S. A. Turubanova, M. C. Hansen, B. Adusei, M. Broich, A. Altstatt, L. Mane, C. O. Justice, Quantifying forest cover loss in Democratic Republic of the Congo,

2000–2010, with Landsat ETM+ data. *Remote Sens. Environ.* **122**, 106–116 (2012). doi:10.1016/j.rse.2011.08.027</jrn>

<jrn>51. M. C. Hansen, P. V. Potapov, R. Moore, M. Hancher, S. A. Turubanova, A. Tyukavina, D. Thau, S. V. Stehman, S. J. Goetz, T. R. Loveland, A. Kommareddy, A. Egorov, L. Chini, C. O. Justice, J. R. G. Townshend, High-resolution global maps of 21st-century forest cover change. *Science* **342**, 850–853 (2013). doi:10.1126/science.1244693 Medline</jrn>

<jrn>52. G. Azzari, D. B. Lobell, Landsat-based classification in the cloud: An opportunity for a paradigm shift in land cover monitoring. *Remote Sens. Environ.* **202**, 64–74 (2017). doi:10.1016/j.rse.2017.05.025</jrn>

<jrn>53. V. Kovalskyy, D. P. Roy, The global availability of Landsat 5 TM and Landsat 7 ETM+ land surface observations and implications for global 30m Landsat data product generation. *Remote Sens. Environ.* **130**, 280–293 (2013). doi:10.1016/j.rse.2012.12.003</jrn>

<jrn>54. N. Saintilan, N. C. Wilson, K. Rogers, A. Rajkaran, K. W. Krauss, Mangrove expansion and salt marsh decline at mangrove poleward limits. *Glob. Change Biol.* **20**, 147–157 (2014). doi:10.1111/gcb.12341 Medline</jrn>

<jrn>55. J. Takaku, T. Tadono, K. Tsutsui, Generation of high resolution global DSM from ALOS PRISM. *Int. Arch. Photogramm. Remote Sens. Spat. Inf. Sci* **XL-4**, 243–248 (2014). doi:10.5194/isprsarchives-XL-4-243-2014</jrn>

<jrn>56. M. N. Wright, A. Ziegler, ranger: A Fast Implementation of Random Forests for High Dimensional Data in C++ and R. *J. Stat. Softw.* **77**, 1–17 (2017). doi:10.18637/jss.v077.i01</jrn>

<other>57. J. R. Eastman, J. Toledano, “Phase 3 Extension to the Mapping of Tropical Pond Aquaculture, Mangroves and Coastal Wetlands” (Clark Labs, Aquaculture and Coastal Habitats Report No. 6, 2020).</other>

<jrn>58. R. M. Fuller, G. M. Smith, B. J. Devereux, The characterisation and measurement of land cover change through remote sensing: Problems in operational applications? *ITC J.* **4**, 243–253 (2003). doi:10.1016/S0303-2434(03)00004-7</jrn>

<jrn>59. C. K. F. Lee, E. Nicholson, C. Duncan, N. J. Murray, Estimating changes and trends in ecosystem extent with dense time-series satellite remote sensing. *Conserv. Biol.* **35**, 325–335 (2021). doi:10.1111/cobi.13520 Medline</jrn>

<jrn>60. P. Olofsson, G. M. Foody, M. Herold, S. V. Stehman, C. E. Woodcock, M. A. Wulder, Good practices for estimating area and assessing accuracy of land change. *Remote Sens. Environ.* **148**, 42–57 (2014). doi:10.1016/j.rse.2014.02.015</jrn>

<eref>61. M. C. Hansen, P. Potapov, A. Tyukavina, Comment on “Tropical forests are a net carbon source based on aboveground measurements of gain and loss”. *Science* **363**, eaar3629 (2019). doi:10.1126/science.aar3629 Medline</eref>

<bok>62. R. G. Congalton, K. Green, *Assessing the Accuracy of Remotely Sensed Data: Principles and Practices* (CRC Press, 2008).</bok>

<jrn>63. R. Congalton, J. Gu, K. Yadav, P. Thenkabail, M. Ozdogan, Global Land Cover Mapping: A Review and Uncertainty Analysis. *Remote Sens. (Basel)* **6**, 12070–12093 (2014). doi:10.3390/rs61212070</jrn>

<jrn>64. P. Olofsson, G. M. Foody, S. V. Stehman, C. E. Woodcock, Making better use of accuracy data in land change studies: Estimating accuracy and area and quantifying uncertainty using stratified estimation. *Remote Sens. Environ.* **129**, 122–131 (2013). doi:10.1016/j.rse.2012.10.031</jrn>

<jrn>65. S. V. Stehman, J. D. Wickham, Assessing accuracy of net change derived from land cover maps. *Photogramm. Eng. Remote Sensing* **72**, 175–185 (2006). doi:10.14358/PERS.72.2.175</jrn>

<jrn>66. B. Efron, R. Tibshirani, Improvements on cross-validation: The 632+ bootstrap method. *J. Am. Stat. Assoc.* **92**, 548–560 (1997).</jrn>

<jrn>67. S. K. McFeeters, The use of the Normalized Difference Water Index (NDWI) in the delineation of open water features. *Int. J. Remote Sens.* **17**, 1425–1432 (1996). doi:10.1080/01431169608948714</jrn>

<jrn>68. H. Xu, Modification of normalised difference water index (NDWI) to enhance open water features in remotely sensed imagery. *Int. J. Remote Sens.* **27**, 3025–3033 (2006). doi:10.1080/01431160600589179</jrn>

<jrn>69. G. L. Feyisa, H. Meilby, R. Fensholt, S. R. Proud, Automated Water Extraction Index: A new technique for surface water mapping using Landsat imagery. *Remote Sens. Environ.* **140**, 23–35 (2014). doi:10.1016/j.rse.2013.08.029</jrn>

<jrn>70. M. B. Lyons, D. A. Keith, S. R. Phinn, T. J. Mason, J. Elith, A comparison of resampling methods for remote sensing classification and accuracy assessment. *Remote Sens. Environ.* **208**, 145–153 (2018). doi:10.1016/j.rse.2018.02.026</jrn>

<jrn>71. G. P. Asner, D. E. Knapp, E. N. Broadbent, P. J. C. Oliveira, M. Keller, J. N. Silva, Selective logging in the Brazilian Amazon. *Science* **310**, 480–482 (2005). doi:10.1126/science.1118051 Medline</jrn>

<eref>72. Flanders Marine Institute, Union of the ESRI Country shapefile and the Exclusive Economic Zones (2020); https://doi.org/10.14284/403.</eref>

<jrn>73. M. D. Spalding, H. E. Fox, G. R. Allen, N. Davidson, Z. A. Ferdaña, M. Finlayson, B. S. Halpern, M. A. Jorge, A. Lombana, S. A. Lourie, K. D. Martin, E. McManus, J. Molnar, C. A. Recchia, J. Robertson, Marine ecoregions of the world: A bioregionalization of coastal and shelf areas. *Bioscience* **57**, 573–583 (2007). doi:10.1641/B570707</jrn>

<jrn>74. D. R. Richards, D. A. Friess, Rates and drivers of mangrove deforestation in Southeast Asia, 2000-2012. *Proc. Natl. Acad. Sci. U.S.A.* **113**, 344–349 (2016). doi:10.1073/pnas.1510272113 Medline</jrn>

<jrn>75. J. Franklin, J. M. Serra-Diaz, A. D. Syphard, H. M. Regan, Global change and terrestrial plant community dynamics. *Proc. Natl. Acad. Sci. U.S.A.* **113**, 3725–3734 (2016). doi:10.1073/pnas.1519911113 Medline</jrn>